Article

A Method for the Integrated Optimal Design of Multiphase Pump Based on the Sparse Grid Model

Cancan Peng [1],*[iD], **Xiaodong Zhang** [1], **Yongqiang Chen** [2], **Yan Gong** [1], **Hedong Li** [1] **and Shaoxiong Huang** [1]

1 Institution of Mechanical and Electrical Engineering, Southwest Petroleum University, Chengdu 610500, China; zxd123420@126.com (X.Z.); gongyan0101@163.com (Y.G.); 202031030010@stu.swpu.edu.cn (H.L.); xkarz52116@outlook.com (S.H.)
2 Jiyuan Huaxin Petroleum Machinery Co., Ltd., Jiyuan 454650, China; xiaoxuan425@sina.com
* Correspondence: 201811000059@stu.swpu.edu.cn

Abstract: Multiphase pumps are used as an important tool for natural gas hydrate extraction owing to their excellent gas–liquid mixing and transport properties. This paper proposes an adaptive response surface-based integrated optimization design method. A model pump is designed based on the axial flow pump design theory. The model pump is numerically simulated and analyzed to obtain its performance parameters. Then the structural and performance parameters of the pump are parameterized to establish a closed-loop input–output system. Based on this closed-loop system, a sensitivity analysis is performed on the structural parameters of the impeller and guide vane, and the parameters that affect the performance of the gas–liquid hybrid pump the most are derived. The Sparse Grid method was introduced to design the experiment and construct the approximate model. The structural parameters of the impeller and guide vane are used as design variables to optimize the pressure increment and efficiency of the pump. After optimization, the pressure increment of the multiphase pump was increased by 10.78 KPa and the efficiency was increased by 0.89% compared to the original model. Finally, we validate the accuracy of the optimized model with tests.

Keywords: multiphase pump; integrated design; Sparse Grid method; numerical analysis; flow field characteristics

1. Introduction

With the development of the world and the advancement of technology, traditional resources such as coal and oil can no longer meet people's pursuit of a green, eco-friendly, and low-carbon lifestyle. Natural gas hydrates are a clean energy resource and have huge global reserves of approximately 1.5×10^{16} m³ [1]. More than 230 hydrate deposits have been discovered globally on the seafloor and in permafrost zones, where low-temperature and high-pressure conditions are suitable for the formation of natural gas hydrates [2]. Currently, natural gas hydrate extraction relies heavily on a hydraulic lift and requires a substantial reduction in downhole pressure to prevent the collapse of the seabed [3]. Traditional axial flow pumps are effective in reducing downhole pressure and perform well with liquid media but are less effective in lifting mixed media such as natural gas hydrates. Multiphase pumps are multiphase fluid transfer devices that play a critical role in the hydraulic lift of gas hydrates. Therefore, research on downhole multiphase pumps is very important.

In recent years, several scholars have investigated numerical simulation methods and internal flow characteristics of multiphase pumps. Suh et al. [4] proposed a developed Euler–Euler method to investigate the effect of different GVF, interphase forces, and bubble diameter on the internal flow characteristics of the multiphase pump. Yu et al. [5,6], Liu et al. [7], and Zhang et al. [8] have studied the interphase forces and obtained a rule of influence between the variation of the interphase forces and the flow field characteristics of the multiphase pump. Zhang et al. [9] applied a non-uniform bubble model to the

numerical simulation process of a multiphase pump. The obtained results of the non-uniform bubble model did not differ much from those of the conventional model at low GVF. However, when the GVF is high, the numerical result of the non-uniform bubble model is closer to the experimental data. Li et al. [10] investigated the distribution of bubbles in a multiphase pump. The size of bubbles was calculated according to the bubble number density equation, and the distribution characteristics of bubbles at different GVF were analyzed to obtain the movement pattern of bubbles in the impeller and guide vane. Zhang et al. [11] analyzed the formation process of the gas pocket in the multiphase pump through non-constant numerical simulations and visualized experiments, and the results of the study provide some guidance for the future design of multiphase pump impellers. Wang et al., Huang et al., Jiang et al., and Shi et al. [12–15] studied the flow characteristics of the multiphase pump from the perspective of energy loss and obtained the influence law of structure parameters and working condition parameters on the performance of the multiphase pump. Xu et al. [16] studied the internal flow pattern of a multiphase pump and developed a multiphase pump with splitting vanes. The efficiency and head of the pump were improved, which provided guidance for the further design and optimization of the multiphase pump. Yu et al. [17] analyzed the transport process of a non-stationary multiphase pump using a two-fluid model and found the main causes of pressure and head fluctuations in a multiphase pump. Xu et al. [18] and Zhang et al. [19] investigated the pressure pulsation characteristics of the multiphase pump and obtained the distribution and variation pattern of pressure fluctuations in the multiphase pump. Zhang et al. [20] and Shi et al. [21] studied the tip clearance of the multiphase pump and obtained the effect of tip clearance on energy characteristics, flow characteristics, and pressure fluctuations, respectively. Shi et al. [22] and Li et al. [23] investigated the effect of GVF on the energy conversion characteristics, pressure fluctuations, blade surface load, gas distribution, and external characteristics of a multiphase pump. Others have investigated the performance of the multiphase pump under high GVF conditions. Zhang et al. [24] proposed improvements to the performance of the multiphase pump under high GVF conditions. Yang et al. [25] developed a comprehensive SRMP model to predict the performance of pumps at high GVF, which included steady-state behavior and transient performance during pump operation. Shi et al. [26,27] and Liu et al. [28] investigated the cavitation effects of the multiphase pump, and the effect of different GVFs on the energy loss characteristics for each cavitation phase was obtained.

　　There have also been some studies on the design and optimization of multiphase pumps. Zhang et al. [29] proposed a 3D Blade Hydraulic Design Method to design the impeller of a multiphase pump. The new impeller is more conducive for the transport of gas–liquid mixtures and is more suitable for large volume rate conditions. Cao et al. [30] proposed a method that combines Inverse Design and CFD Analysis. The mixture of the two species is considered a homogeneous fluid, and the geometry of the vanes is designed according to the velocity–torque distribution. This method designed a pump that can operate over a wide range of flow rates. Xiao et al. [31] proposed a controlled velocity moment design method for multiphase pumps combined with the singularity method, and the optimized design has a large performance improvement over the model pump. Liu et al. [32] proposed a hydraulic design method with a controllable blade angle to design and optimize multiphase pumps, and the optimized GVF and pressure distribution are more uniform. The transmission performance of the multiphase pump was improved. Shi et al. [33], Kim et al. [34], and Suh et al. [35] all used the design method of orthogonal experiments to optimize the structural parameters of the multiphase pump, and the results show that the head and efficiency of the optimized multiphase were improved, respectively. Zhang et al. [36] proposed an optimization method combining an artificial neural network and non-dominated sorting genetic algorithm-ii to optimize the structural parameters of a multiphase pump, and the head and efficiency of the optimized pump were greatly improved compared with the original model pump. Liu et al. [37] presented a method for optimizing the design of multi-stage multiphase pumps based on the Oseen vortex. The

method can predict the smooth velocity moment downstream of the impeller and apply it to the optimization of the inlet vane angle of the impeller in the next stage. They carried out a case study of a three-stage multiphase pump, in which the head and efficiency of the optimized pump were slightly improved.

In general, scholars have conducted a lot of research on the internal flow characteristics of the multiphase pump, but less research has been conducted on the design of the multiphase pump blades. In this paper, an integrated optimal design based on the adaptive response surface method is proposed, which provides a new approach to thinking about the design method of multiphase pumps. The chapters of this paper are organized as follows. In Chapter 2, an original model is designed based on the design theory of the axial flow pump. In Chapter 3, we start with a numerical simulation of the original model to obtain its pressure increment and efficiency. The shape parameters of the original model and the resulting parameters of the numerical simulation are parametrized to create a closed-loop calculation system. Based on the closed-loop calculation system, parameter correlation analysis is carried out to obtain several parameters that have the greatest influence on the performance of the multiphase pump. Next, we carried out the experimental design of the parameters and the construction of the approximate model based on the closed-loop calculation system. The optimal solution was obtained by optimizing the approximate model using the multi-objective genetic algorithm (MOGA) method. In Chapter 4, we compare the flow field characteristics of the model before and after the optimization. In Chapter 5, an experimental test is carried out to verify the accuracy of the numerical simulations of the optimized model. In Chapter 6, we summarize the work in the full text.

2. Design and Calculation of the Original Model

The working parameters for the blade design of a multiphase pump are shown in Table 1.

Table 1. Multiphase pump design working parameters.

Design Parameter	Value	Unit
Rotation speed	4500	rpm/min
Flow rate	35	L/s
Head	20	m
Specific speed	325	

The calculation formula of specific speed is shown as follows.

$$n_s = \frac{3.65n\sqrt{Q}}{H^{3/4}},\tag{1}$$

where n is the rotation speed, Q is the flow rate, and H is the head.

(1) Head coefficient Ψ

$$\Psi = gH/U_t^2,\tag{2}$$

where h is the head, U_t is the circumferential velocity of the shroud, and g is the gravitational acceleration.

(2) Inlet flow coefficient Φ

$$\Phi = V_m/U_t,\tag{3}$$

where V_m is the axial component of absolute velocity. The flow coefficient has a great influence on the efficiency of the pump. Each airfoil corresponds to an optimal flow coefficient range.

(3) Shroud diameter a_1

$$a_1 = \frac{60U_t}{n\pi},\tag{4}$$

The shroud diameter is determined by the head coefficient and should meet the corresponding flow coefficient requirements. For the multiphase pump, due to the compressibility of the gas, the volume flow of the gas–liquid mixture decreases from the inlet to the outlet of the pump impeller, so the impeller diameter at the rear end should be smaller than that in the first half.

(4) Inlet hub ratio h_t and Hub inlet diameter a_2

Inlet hub ratio h_t is the ratio of hub inlet diameter to shroud diameter.

$$a_2 = a_1 h_t, \tag{5}$$

(5) Shroud length diameter ratio h_v and Hub length of impeller a_4

$$a_4 = h_v a_1, \tag{6}$$

(6) Hub half cone angle γ and Hub outlet diameter a_3

$$a_3 = a_2 + 2a_4 tan\gamma, \tag{7}$$

where a_4 is the axial length of the impeller and γ is the half cone angle of the hub.

A conical hub is generally used for the multiphase pump. This structure can avoid the reduction of the velocity component on the shaft surface caused by gas compression.

(7) Hub inlet flow angle a_6

$$a_6 = a_6' + \Delta a_6, \tag{8}$$

where a_6' is the inlet angle and $\triangle a_6$ is the attack angle.

In the design process, the inlet flow angle is calculated according to the inlet speed and circumferential speed.

$$tana_6 = V/U_t, \tag{9}$$

where V is the velocity at which the fluid enters the impeller.

Then, according to the principle of equal radial guide path, the flow angle of the blade inlet at other radial positions is determined.

$$Const = rtana_6, \tag{10}$$

where r is the radius of the blade and a_6 means the hub inlet flow angle.

(8) Hub outlet flow angle a_7

According to the design theory of axial flow pump, the blade outlet installation angle (a_7) can be calculated, and then the blade outlet flow angle of other diameters can be determined according to the principle of equal diameter and guide path.

(9) Tip clearance a_9

The tip clearance is the radial clearance between the impeller shroud and the pump shell. Excessive clearance will lead to increased leakage. In this paper, the clearance is taken as 0.5 mm.

(10) Maximum blade thickness

$$\delta_{max} = (0.012 \sim 0.015)a_1 \sqrt{H}, \tag{11}$$

where δ_{max} is the maximum thickness of the hub and H is the head.

After the above design parameters are determined, the impeller of the multiphase pump is designed, and the parameter of the blade is shown in Table 2.

Table 2. Design and construction parameters of the multiphase pump.

	Design Parameter	Value	Unit	Expression
Impeller	Head coefficient	0.23		Ψ
	Circumferential velocity of the shroud	29.2	m/s	U_t
	Shroud diameter	0.138	m	a_1
	Inlet hub ratio	0.7		h_t
	Hub inlet diameter	0.096	m	a_2
	Hub half cone angle	7	°	γ
	Shroud length diameter ratio	0.39		h_v
	Hub length of impeller	0.054	m	a_4
	Hub outlet diameter	0.108	m	a_3/P7
	Hub inlet flow angle	16.1	°	a_6/P1
	Shroud inlet flow angle	13.4	°	P2
	Hub outlet flow angle	15.8	°	a_7/P3
	Shroud outlet flow angle	14.4	°	P4
	Number of blades	3		a_5
	Wrap angle	173	°	a_8/P8 (Hub), P9 (Shroud)
Guide vane	Hub inlet diameter	0.108	m	P7
	Hub outlet diameter	0.096	m	-
	Hub inlet flow angle	41.66	°	P5
	Shroud inlet flow angle	36.9	°	P6
	Axial length of guide vane	0.054	m	P10 (inlet position), P11 (outlet position)
	Number of blades	11		-
	Wrap angle	32.73	°	-

The blade is modeled according to the structural parameters of Table 1, and the geometric model is shown in Figure 1.
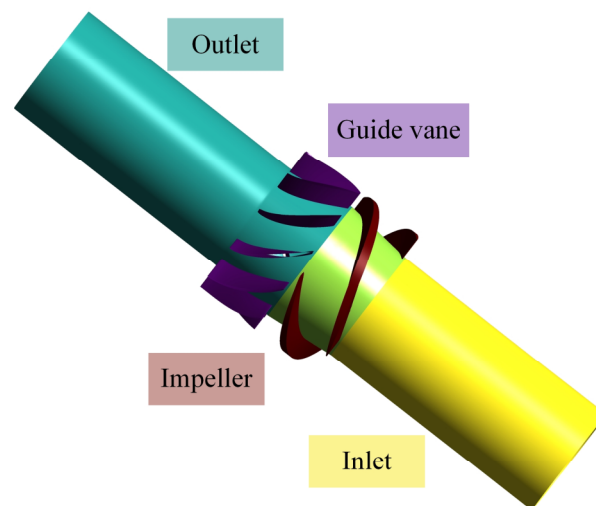
Figure 1. Model diagram of the impeller and guide vane of the multiphase pump.

3. Numerical Simulation and Optimization

3.1. Numerical Simulation of the Original Model

CFD methods are widely used in the fields of turbulence [38], multiphase flow [39], and heat transfer [40] owing to the advantages of low research costs and the ability to simulate complex or ideal processes. In this chapter, the CFD method is used to design, mesh, and numerically simulate an original model of a multiphase pump based on the ANSYS 2020R2 Workbench platform. We consider this process as the creation of an input–output channel. The structural parameters of the original model and the calculated performance parameters are parametrized. We construct a parameter set for the input and output

separately and then connect them via the channels we created earlier. When we modify the input parameter set, and the system automatically applies this computational channel that we established earlier to calculate the output performance parameters. The solution of the data points involved in the parameter correlation analysis, design of experiments, construction of the agent model, and validation of the optimization results required in the following section is carried out on the closed-loop system of this calculation channel. The inner circle of Figure 2 represents our numerical simulation of the original model. The outer ring represents a closed-loop calculation channel created after parameterization of the structural and performance parameters of the multiphase pump.
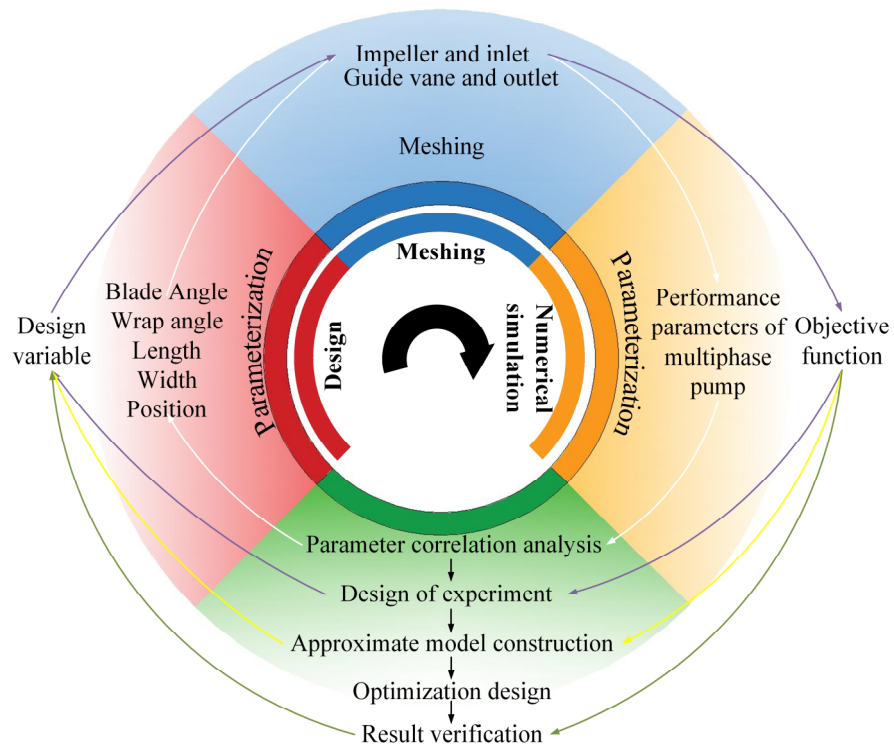

Figure 2. The flow chart of the integrated optimal design approach.

The numerical simulation in this paper is solved by the Euler–Euler method for the gas–liquid two-phase flow model. The gas is considered as a dispersive particle of equal particle size for the solution and the liquid is considered a continuous medium. The two-phase flow model is a non-homogeneous model, which considers the velocity slip and momentum transfer between two phases. The particle model is used for interphase transfer and the Schiller–Nauman model is used for the traction model. The velocity inlet condition and the opening outlet condition are used in the numerical simulation process. The no-slip wall condition is used for the hub and wall, and the counter-rotating wall condition is used for the impeller's shroud. The frozen rotor model is used for the dynamic–static interface. The SST model combines the advantages of the k-ε and k-ω models to provide a more accurate and reliable description of the flow of a fluid and to correspond to a wider range of flow models [41]. In this paper, the SST model is used for the solution of the liquid phase, and the zero-equation model is used for the solution of the gas phase. The convergence residuals are taken as 1×10^{-5}. During the calculation of the numerical simulation, the flow rate changes at the inlet and outlet are detected, and the convergence curve of the residuals is combined to determine whether the calculation process converges.

To ensure the accuracy of the numerical simulation, a mesh-independent analysis is performed. The grid in this paper is refined by controlling the y+ value of the first layer boundary to refine the global grid. The y+ value is taken as 10, and the grid diagram is shown in Figure 3.
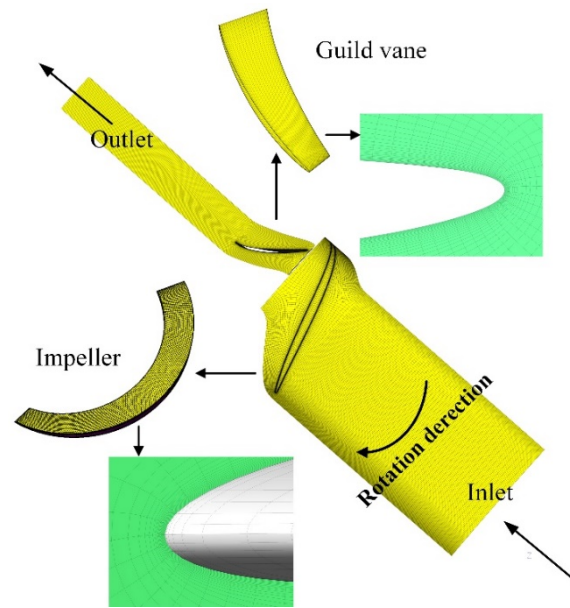
Figure 3. Grids for the numerical simulation the multiphase pump.

The grid-independent analysis was performed for the GVF = 0 working condition. Figure 4 shows that the efficiency and head curves tend to level off when the number of grids reaches 1.96 million, so we use a grid of 1.96 million for the subsequent numerical simulations.
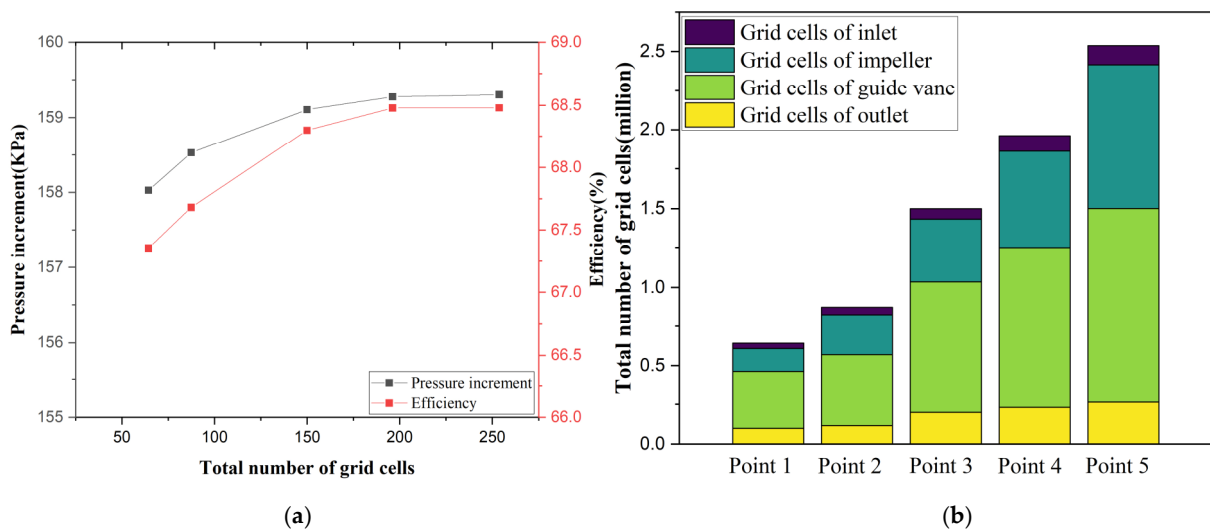

(**a**)   (**b**)

Figure 4. Verification of grid independence for numerical simulation of the multiphase pump. (**a**) Curves of grid number growth with performance parameters; (**b**) comparison of the number of grids in different areas of the multiphase pump.

After numerical calculations, we obtain a pressure increment of 159.3 KPa and an efficiency of 68.48% for the pump under the design conditions.

3.2. Parameter Correlation Analysis

We parameterize the input structural parameters and the output pump performance parameters separately. A calculation channel connecting the input and output parameters is established for the working condition of GVF = 0. Then, a parametric sensitivity analysis is performed on the structural parameters.

The Person correlation coefficient method [42] is a statistical method to measure quantitatively the correlation between variables. It has a wide range of applications in com-

putational linguistics and is mainly used in research on text classification and information extraction. Using the vector space model of feature words, the distance between two pairs of texts is calculated to derive the similarity, which leads to the classification and further study of the text collection.

When calculated for a sample, the magnitude of the Pearson correlation coefficient is determined by the value of σ, which reflects the degree to which the two variables are linearly correlated. σ has a range of values from -1 to $+1$. A correlation coefficient of $+1$ indicates a perfect positive linear correlation between the variables. The Pearson correlation coefficient is calculated as follows [43].

$$\sigma = \frac{\sum XY - \frac{\sum X \sum Y}{N}}{\sqrt{\left(\sum X^2 - \frac{(\sum X)^2}{N}\right)\left(\sum Y^2 - \frac{(\sum Y)^2}{N}\right)}} \tag{12}$$

where variable X is the set of x-coordinates of all points, variable Y is the set of y-coordinates of all points, and N denotes the total number of points.

The Pearson correlation coefficient is the ratio of the product of the covariance and the standard deviation of the two variables and is a dimensionless, standardized covariance. A linear change does not affect the results of the Pearson correlation coefficient. Therefore, a unit change in the horizontal or vertical coordinates does not change the value of σ, so the σ values are comparable for data with different units.

Figure 5 gives the parameter sensitivity relationships between the design parameters and the optimization objectives, in which red and blue colors indicate high correlation and the white color indicates low correlation. The distribution of colors in the graph shows a high correlation between the variables P8, P9, P2, P4, P6, and the optimization objective. Among them, we consider P8 and P9 to be equal, so we finally determine P8, P2, P4, and P6 as the design variables.
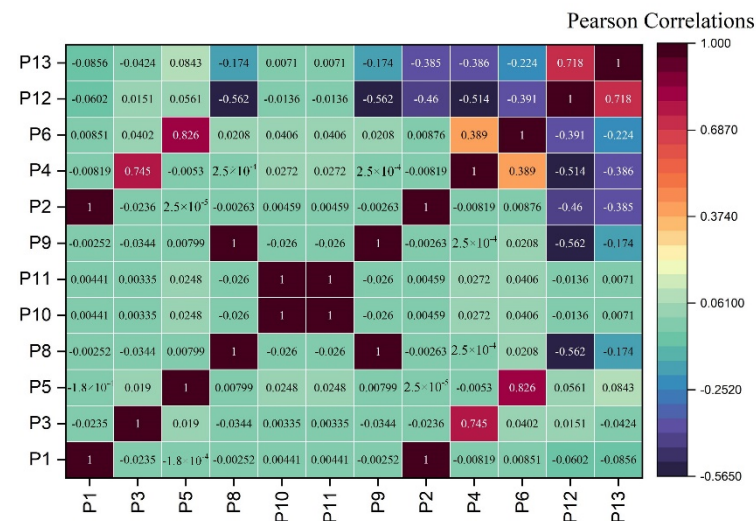

Figure 5. Parameter correlation chart.

3.3. DOE

The Sparse Grid model is a hierarchical Sparse Grid interpolation algorithm based on segmented multilinear basis functions. As its initial sampling points are related to the hierarchical basis functions, the number of sampling points will be significantly reduced compared to a full grid model. The Sparse Grid relies on a hierarchical decomposition

of the underlying approximation space. The hierarchical basis is a function based on the following, which we express in Formula (13).

$$\varphi(x) = \begin{cases} 1 - |x| & x \in [-1, 1] \\ 0 & x \notin [-1, 1] \end{cases}, \tag{13}$$

The basis function builds on this function with the following expression.

$$\varphi_{l,i}(x) = \varphi\left(\frac{x - ih_l}{h_l}\right) \ x \in [x_{l,i} - h_l, x_{l,i} + h_l], \tag{14}$$

where l is the number of levels and i is the space location. Figure 6 shows the basis functions and response space for one-dimensional interpolation at the $l = 3$ condition [44].
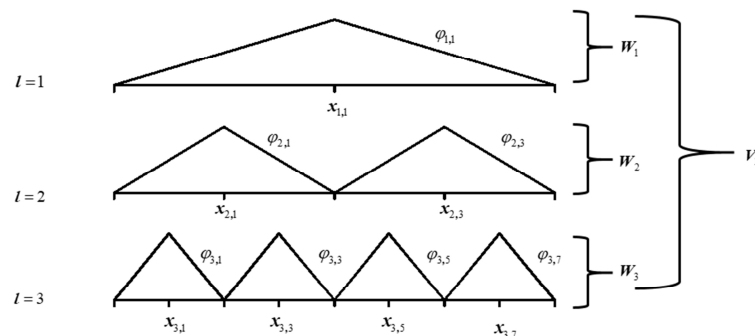

Figure 6. Basis functions and response space for one-dimensional interpolation at $l = 3$ condition.

The layered incremental space is shown in Equation (15)

$$W_l = span\{\varphi_{l,i} : i \in I_l\}$$
$$I_l = \left\{i \in N, 1 \le i \le 2^l - 1\right\} \tag{15}$$

The response function space for the full grid is shown below.

$$V_l = \bigoplus_{k \le l} W_k, \tag{16}$$

The Sparse Grid model, on the other hand, ignores subspaces from the full grid that have less influence on local differences, and its response function space is shown below [37].

$$V_{O,n}^S = \bigoplus_{|i| \le n+d-1} W_l, \tag{17}$$

The one-dimensional interpolation approximation model can be expressed as

$$f(x) \approx u(x) = \sum_{k=1}^{l} \sum_{i \in I_l} \alpha_{k,i} \varphi_{k,i}(x), \tag{18}$$

When dealing with multi-dimensional problems, the Sparse Grid model can significantly reduce the dependence on the sampling points in each dimension and improve computational efficiency. Sparse Grid experimental design enables the construction of experimental designs with fewer points while ensuring that the test points are distributed as evenly as possible in the design space. Compared with CCD and Latin hypercube algorithms, it is less computationally intensive and more efficient. Therefore, the Sparse Grid model is used for the experimental design method in this paper.

The range of values for each parameter of the multiphase pump is shown in Table 3. The experimental design table obtained is shown in Table 4.

Table 3. The range of values of structural parameters.

| Structure Parameters	Lower Value	Upper Value	Unit	Expression
Shroud inlet flow angle of impeller	13	19		P2
Shroud outlet flow angle of impeller	15	21		P4
Wrap angle of impeller	155	195		P8
Shroud inlet angle of guide vane	39	45		P6

Table 4. Experimental design based on the Sparse Grid method.

Name	P2 (°)	P4 (°)	P6 (°)	P8 (°)	Pressure Increment (KPa)	Efficiency (%)
1	16	18	42	175	111.680	47.8541
2	13	18	42	175	117.246	48.8855
3	19	18	42	175	105.822	46.4865
4	16	15	42	175	107.892	47.1617
5	16	21	42	175	116.008	48.7249
6	16	18	39	175	111.877	47.8882
7	16	18	45	175	111.609	47.8679
8	16	18	42	155	148.415	44.3653
9	16	18	42	195	62.7643	43.5081

3.4. Construction of Approximate Models

The Sparse Grid method can provide refinement for continuous parameters, which means that it can automatically optimize itself. The dimensional adaptive algorithm allows it to determine which dimensions are most important to the objective function. When updating the response surface, the Sparse Grid uses an automatic local optimization process to determine the areas of the response surface that are most in need of further optimization. Then, it concentrates refinement points in these regions, allowing for the response surface to reach the specified accuracy faster with fewer design points. This results in a reduction in computational effort.

Figure 7 shows the residual convergence curve for the computation of the Sparse Grid. It can be seen that the head converges faster during the calculation, and the specified convergence requirement is reached at 40 data points. The efficiency comes the convergence requirement at 96 data points. Figure 8 shows the goodness-of-fit curve of the Sparse Grid, which refers to the degree of fit of the regression curve to the observed values. The statistical measure of goodness of fit is the coefficient of determination (also called coefficient of determination) R^2, the maximum value of which is 1. In summary, the goodness of fit is used to measure how well the fitted curve fits the original data, and the closer the data points are to the line y = x, the better the goodness of fit. From the data in Figure 8, we can see that almost all data points are very close to the line y = x, so we can judge that the goodness of fit is very good.
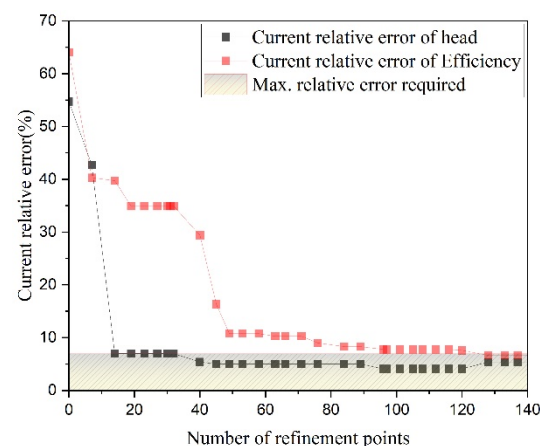
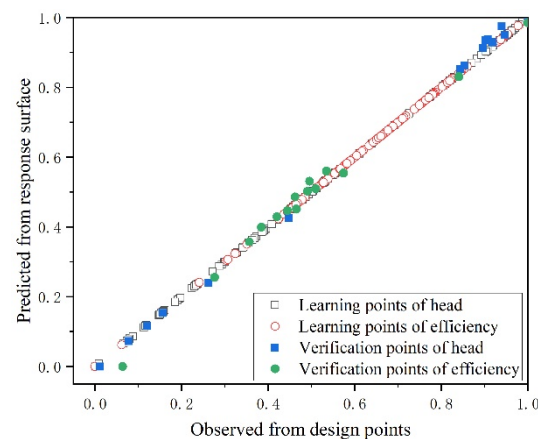**Figure 7.** Convergence curves for the Sparse Grid approximation model.

Figure 8. Goodness of fit curve for the Sparse Grid method.

3.5. Optimization

For the optimization of impeller parameters in this paper, a multi-objective genetic algorithm (MOGA) is used. The estimated number of evaluations is 2000. The number of initial samples is 100. The number of samples per iteration is 100. The maximum allowable Pareto percentage is 70%. The convergence stability percentage is 2%. The maximum number of iterations is 100. When the calculation reaches the 9th iteration step, the calculation converges, and the number of evaluations reaches 823.

The optimal set of Pareto solutions obtained from the optimization is shown in Figure 9. From the data in the figure, it can be seen that when the head increases, the efficiency is decreasing. When the efficiency increases, the head also decreases. The relationship between the two is mutually constrained. The goal of optimization is to maximize both head and efficiency, and we can find the optimal solution that satisfies both goals from these 13 optimization results. The final results of the optimal solutions are shown in Table 5.
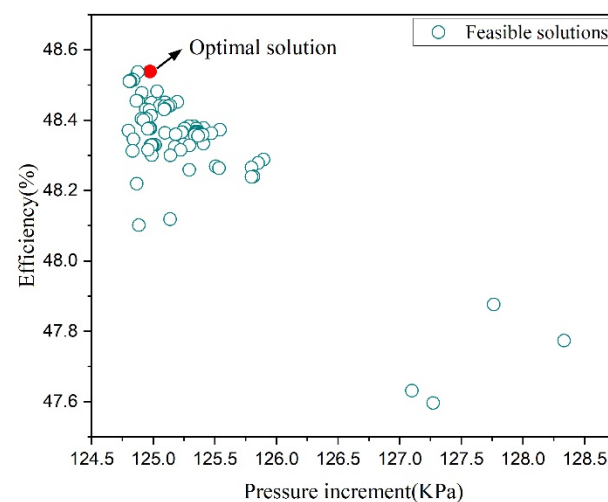

Figure 9. Pareto fronts of the optimization process.

Table 5. Optimization result parameters.

Name	Candidate Point	Calibrated Point of Optimized Model	Unit
P2	13.008	13	°
P4	20.15	20	°
P6	39.494	39.5	°
P8	170.05	170	°
Head	124.87	124.72	KPa
Efficiency	48.455	48.501	%

4. Discussion

We constructed an integrated optimized design model for the multiphase pump and completed the optimized design of the multiphase pump to obtain the optimized model of the multiphase pump structure based on the closed-loop calculation system we built. In this chapter, we compare the models before and after optimization, and analyze the changes in the internal flow field of the two different models.

Figure 10 gives the static pressure distribution of the blade surface under the water condition. Figure 10a,b shows that the area of the high-pressure region of the pressure surface of the optimized model is higher than that of the original model, especially in the position near the leading and trailing edges of the impeller is more obvious. The higher static pressure on the impeller surface indicates that the fluid medium is converted into more energy, so the performance of the impeller is better. Figure 10c,d shows that the pressure change of the suction surface before and after optimization is not obvious. Figure 11 gives the static pressure distribution on the blade surface with GVF = 0.2. From Figure 11a,b, it can be concluded that the optimized blade surface pressure is larger than the original model, and the area of pressure increase is mainly shown in the outer edge of the impeller pressure surface, which shows that the optimized blade has better energy conversion characteristics. From Figure 11c,d, it can be concluded that the pressure change of the optimized suction surface is small, and there is a slight increase at the inlet of the impeller.
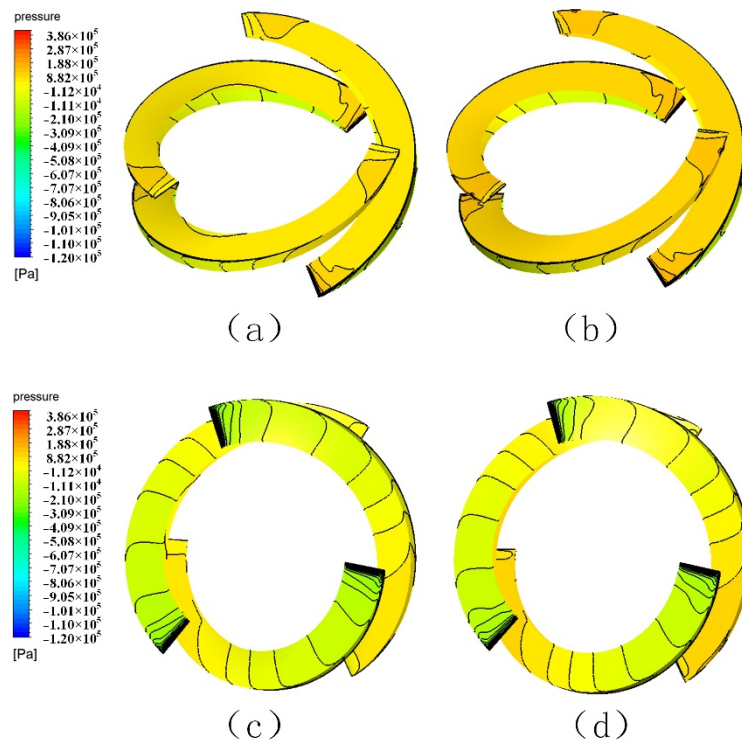

Figure 10. Surface static pressure distribution of the impeller in water condition. (**a**) Pressure side of original model; (**b**) pressure side of optimized model; (**c**) suction side of original model; (**d**) suction side of optimized model.
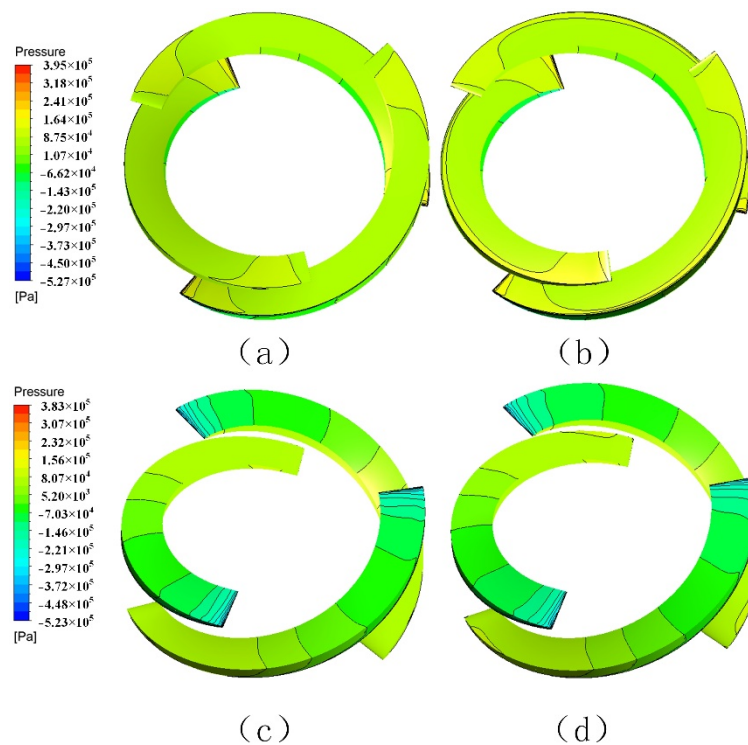
Figure 11. Distribution of surface static pressure on impeller at GVF = 20% working condition. (**a**) Pressure side of original model; (**b**) pressure side of optimized model; **(c)** suction side of original model; (**d**) suction side of optimized model.

Figure 12 gives the distribution of blade load under the water working condition. We can conclude that the surface load of the blade increases with the increase of span-wise and then decreases, and the pressure in the outer area of the blade is obviously higher than that in the inner area. It can be seen from the figure that the pressure of the blade suction surface is lower and the pressure difference is larger after optimization. Therefore, it can produce higher head. The area enclosed by the optimized blade load curve is larger than that of the original model, so the energy conversion characteristics of the blade are better. As can be seen from Figure 13, the overall surface load of the blade at GVF = 0.2 is lower than the water working condition, and the changing trend of the curve is not much different from the water condition. The energy conversion characteristics of the optimized impeller are better.
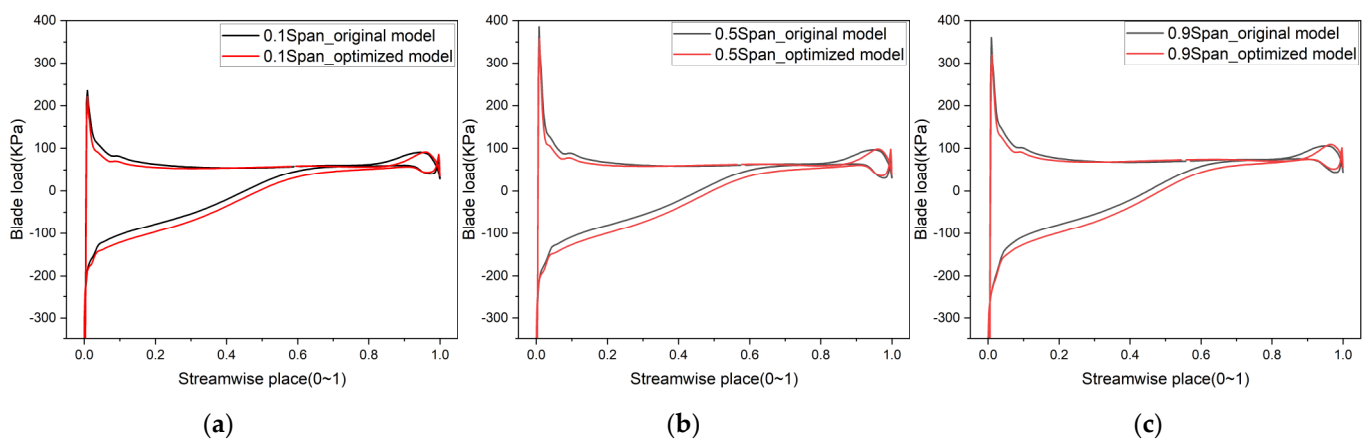

Figure 12. Distribution of blade loads along the span-wise place under the water condition. (**a**) 0.1 span, (**b**) 0.5 span, and (**c**) 0.9 span.
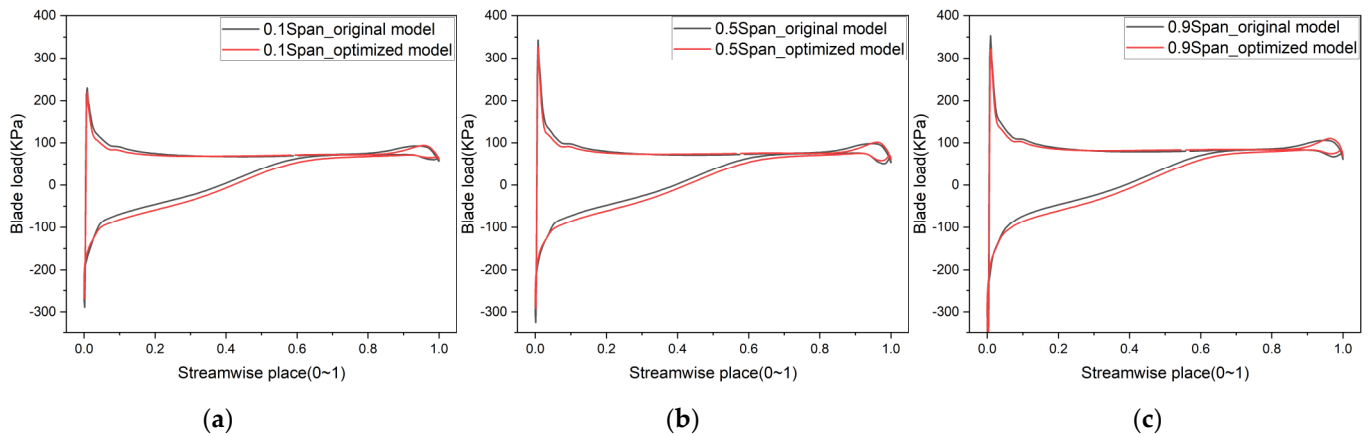
Figure 13. Distribution of blade loads along the span-wise place at 20%GVF condition. (**a**) 0.1 span, (**b**) 0.5 span, and (**c**) 0.9 span.

A swirling strength criterion was used to construct a vortex intensity cloud in the impeller region. Figure 14 gives the distribution of the vortex structure under the different working conditions. It can be concluded that the internal vortex of the multiphase pump is mainly caused by the impeller rotation, which is mainly distributed at the impeller inlet, outlet, and between the gap of the impeller and the shroud. From Figure 14a,e, it can be concluded that the vortex length d_2 at the blade exit of the optimized model is smaller than d_1 of the original model. The vortex intensities in Figure 14f–h are smaller than those in Figure 14b–d. This indicates that the optimization achieved better results.
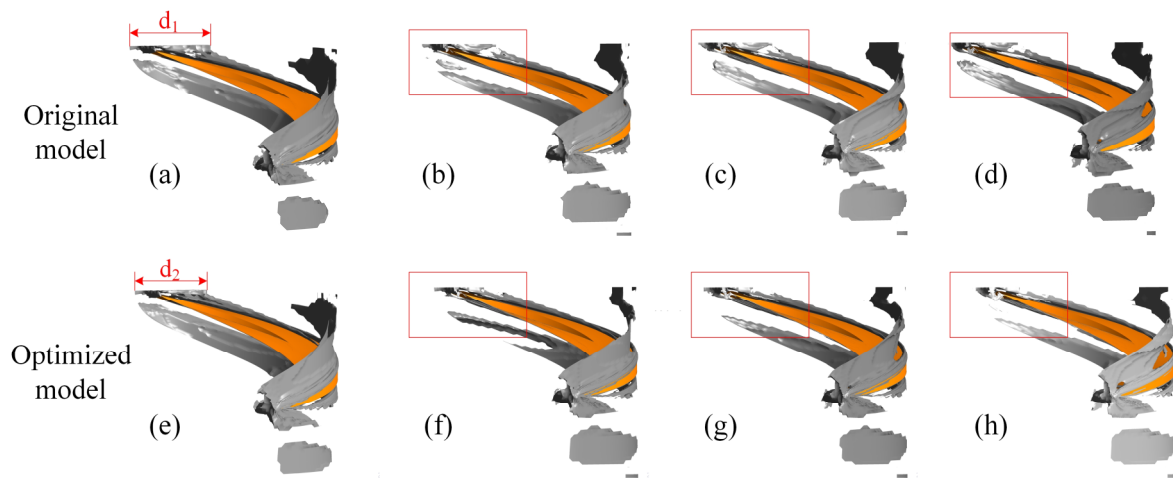

Figure 14. Vortex distribution diagram of the optimized model and the original model. (**a**) GVF = 0 of original model; (**b**) GVF = 10% of original model; (**c**) GVF = 20% of original model; (**d**) GVF = 30% of original model; (**e**) GVF = 0 of optimized model; (**f**) GVF = 10% of optimized model; (**g**) GVF = 20% of optimized model; (**h**) GVF = 30% of optimized model.

The distributions of turbulent energy dissipation rates for the original and optimized models under the water condition are given in Figure 15. The overall turbulent energy dissipation of the optimized model is lower than that of the original model, and the dissipation in both the outlet region shown in Figure 15a and the inlet region shown in Figure 15b of the impeller is improved. The turbulent energy dissipation rate distribution of the impeller and guide vane for GVF = 0.2 is presented in Figure 16. The turbulent energy dissipation at the intersection of the impeller and guide vane is significantly improved by the optimized model. The dissipation in the flow channel region in the middle of the impeller also becomes smaller. It indicates that the optimized performance is better.
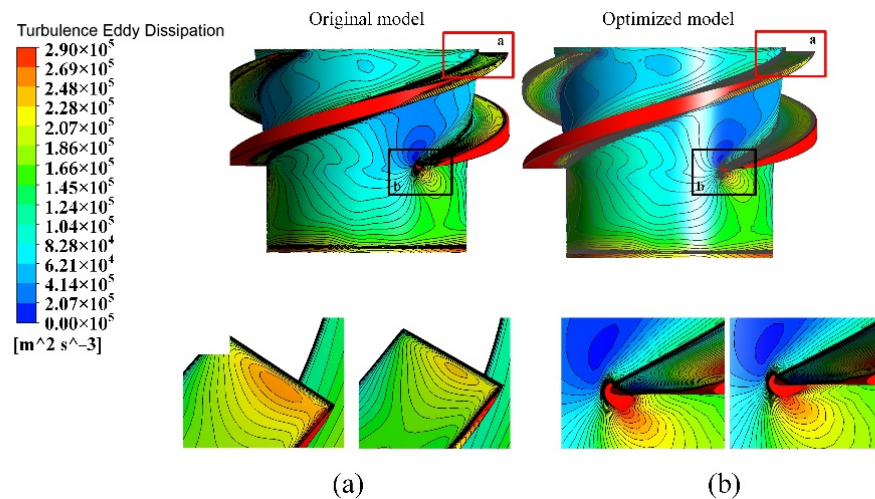
Figure 15. (**a**,**b**) Distribution of turbulent energy dissipation rate under the water condition.
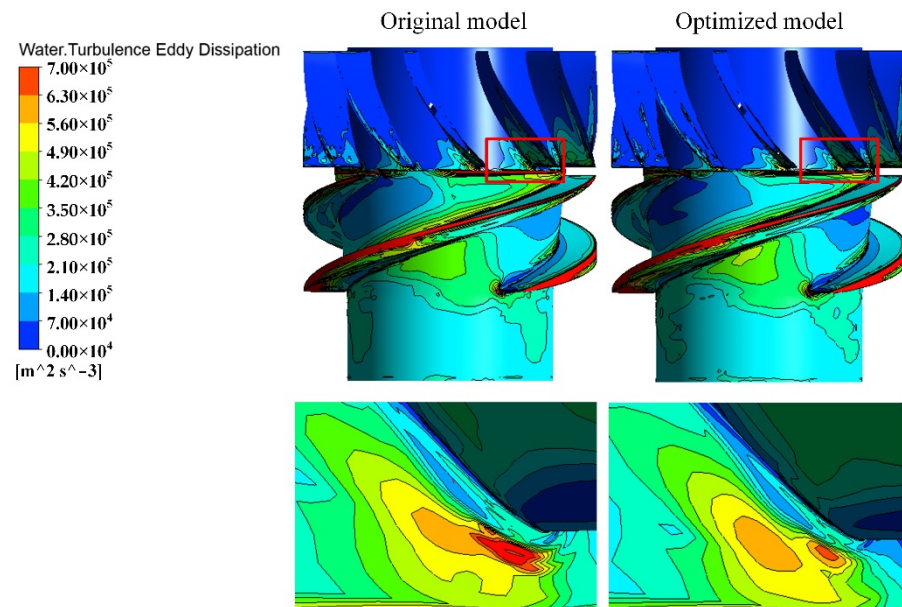

Figure 16. Distribution of turbulent energy dissipation rate under the 20%GVF condition.

Figure 17 provides an internal flow diagram of the impeller and guide vane of a multiphase pump under the water conditions. We can conclude that the flow velocity on the blade surface increases from the hub to the shroud. Compared to the original model, the flow velocity in the impeller region of the optimized model decreases, and the flow velocity in the guide vane region increases. The increased velocity in the guide vane region leads to more severe flow separation, especially near the hub surface. The increased flow velocity results in higher kinetic energy, which is the main reason for the increased head of the optimized multiphase pump. Figure 18 shows the flow lines inside the multiphase pump and guide vane for the condition of 20%GVF. Due to the increased GVF, the flow velocity of the liquid in both the impeller and the guide vane is lower than in the water condition, which leads to a reduction in the performance of the multiphase pump. The optimized model has a lower flow rate in the impeller and a higher flow rate in the guide vane, with increased flow separation near the hub side. This is consistent with the results for the water condition.

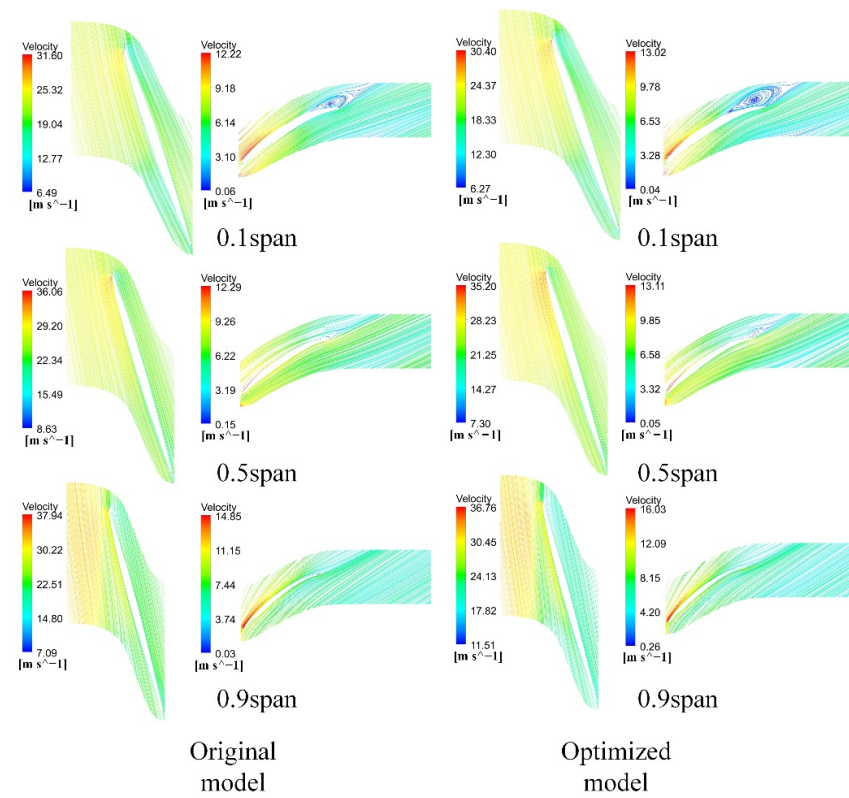**Figure 17.** Streamline distribution of impeller and guide vane before and after optimization under the water condition.
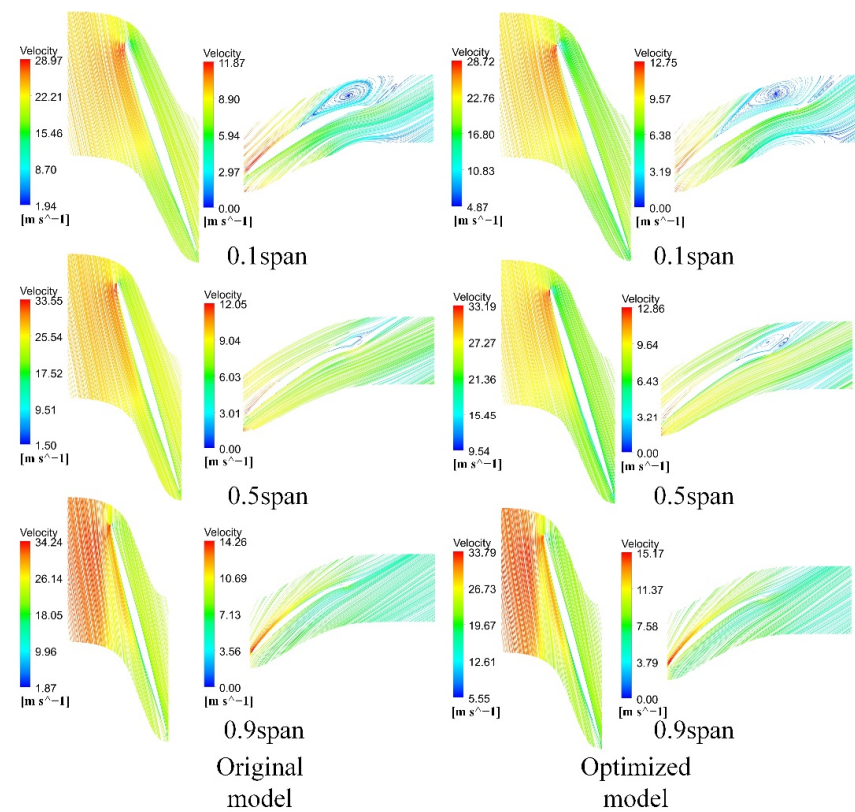

Figure 18. Streamline distribution of impeller and guide vane before and after optimization under the 20%GVF condition.

Figure 19 shows the performance curves of the multiphase pump for different GVF cases. When GVF = 0, the flow-head curve of the multiphase pump shows an obvious hump trend, and the efficiency curve shows a trend of first increasing and then decreasing, which is consistent with the trend of the performance curve of the general axial flow pump. When the gas content gradually increases from 0.0 to 0.3, the optimized model has a higher head than the original model. When the flow rate is small, the efficiency change is not obvious. When the flow rate is larger than the design condition, the optimized model has higher efficiency than the original model. The larger the flow rate is, the more obvious the efficiency improvement is.
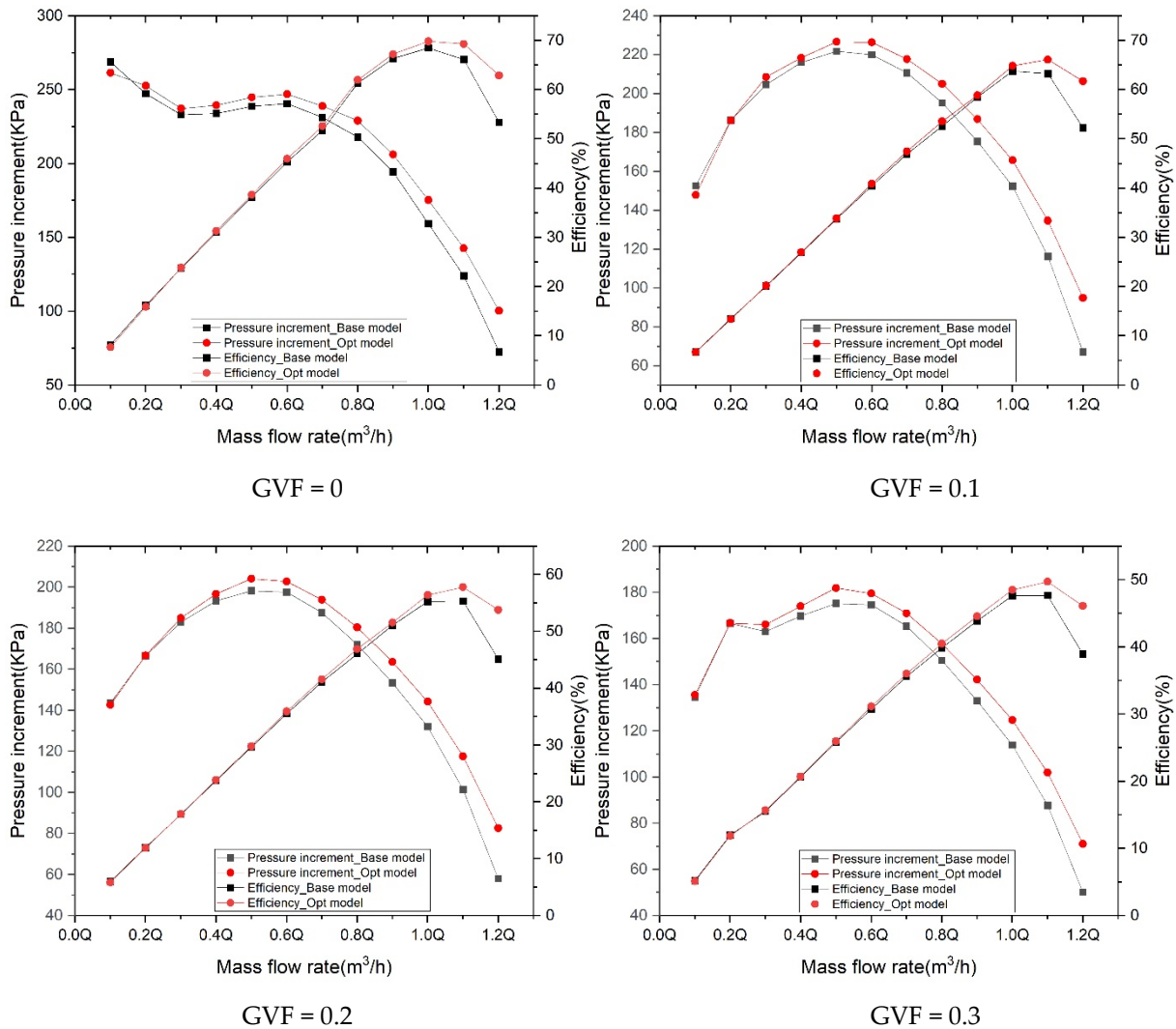

GVF = 0

GVF = 0.1

GVF = 0.2

GVF = 0.3

Figure 19. Characteristic curves of the multiphase pump under different working conditions.

A comparison of our work with other similar works is given in Table 6. The optimization results show an increase in pressure increment and efficiency of 9.4% and 1.8%, respectively. Our working conditions and specific size are different, so there will be some differences in the results. However, we used an integrated design–grid–numerical simulation approach for the optimization process. Only an initial set of data must be calculated to build up a computational framework. Then, the design of experiments, the construction of an approximate model, and the relevant parameters of the optimization method are set to produce the optimal solution. Such design methods are less computationally intensive and more intelligent than their work. Therefore, we believe that the integrated optimization design method proposed in this paper is effective.

Table 6. A comparison of our work and similar works.

		Ming Liu [32]	Zhang [36]	Kim [34]	Suh [35]	Our Work
Optimization process		Step by step				Integrated
Working Condition		GVF = 0 ~10%	GVF = 0 ~40%	GVF = 0	GVF = 0 ~15%	GVF = 30%
Blade size	Diameter	0.15 m	-	0.15 m	0.15 m	0.138 m
	Length	0.075 m	-	0.075 m	-	0.054 m
Pressure Increment (Growth Value/Percentage)		12.8 KPa/-	-/10%	30.9 KPa/-	48.89 KPa/-	10.78 KPa/9.4%
Efficiency (Growth Value/Percentage)		-/-	-/3%	1.9%/-	1.78%/-	0.892%/1.8%

5. Experimental Validation

In order to verify the accuracy of our optimization scheme, a multiphase pump performance test rig was set up to test the performance of the optimized blades. The flow chart of the experiment is shown in Figure 20, and the process of the experiment is shown in Figure 21.

We tested the performance of multiphase pumps under the water condition and GVF = 0.2 condition. The performance curves are shown in Figure 22. The process of numerical simulation is idealized for individual blades and does not take into account the errors caused by the friction between bearings, packing seals, and shafts that exist in the real experimental process. The performance parameters obtained from the tests are slightly lower compared to the results obtained from numerical simulation, which are within the acceptable range. Therefore, we consider that the integrated and optimized design approach used in this paper is effective.
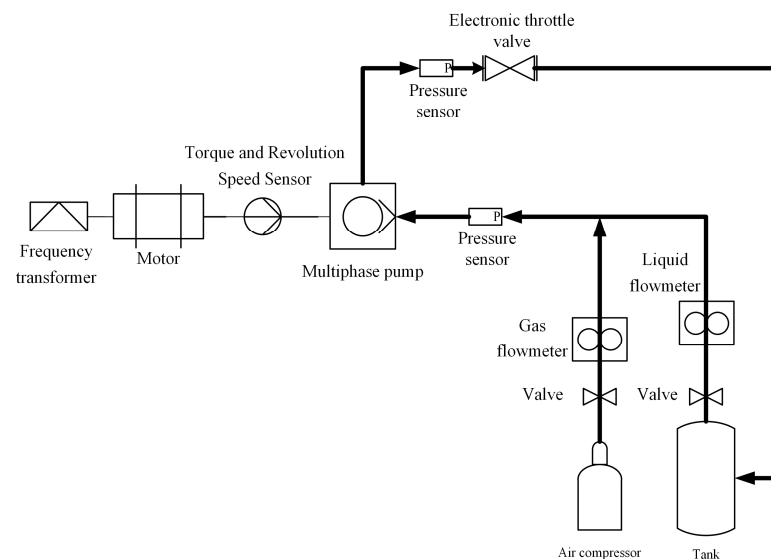

Figure 20. Experimental scheme for the multiphase pump.

Figure 21. Experimental process diagram for the multiphase pump. (1) Motor; (2) frequency transformer; (3) torque and revolution speed sensor; (4) multiphase pump; (5) pressure sensor; (6) liquid flowmeter; (7) gas flowmeter; (8) air compressor; (9) guide vane; (10) impeller; (11) electronic throttle valve; (12) tank; (13) outlet pipe; (14) valve; (15) inlet pipe.
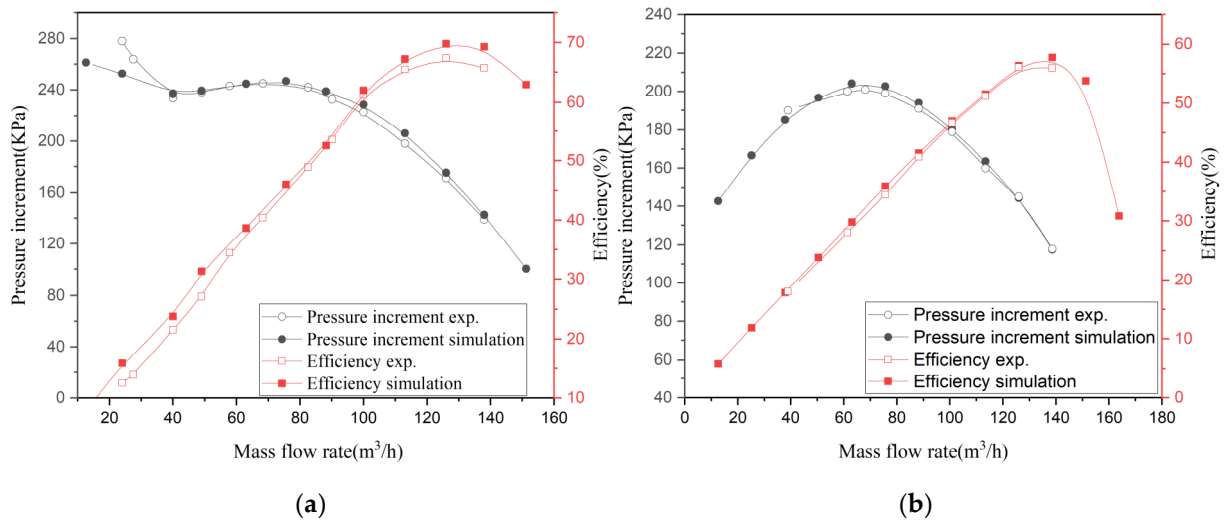

(**a**)

(**b**)

Figure 22. Experimental results of the multiphase pump performance parameters compared with simulation results. (**a**) The water condition; (**b**) GVF = 20%.

6. Conclusions

Firstly, this paper completes the design and numerical simulation of a multiphase pump and derives several pump performance parameters for the water condition. The structural parameters of the blade and the parameters of the results obtained from the numerical simulations are parametrized. A framework integrating the design–meshing–numerical simulation is built up. Within this framework, a parametric correlation analysis was carried out to obtain the parameters that have the greatest influence on the performance of the multiphase pump. They are the shroud inlet angle, the shroud outlet angle, the wrap angle of the impeller, and the shroud inlet angle of the guide vane. Then, the design

of experiments and approximate model building was carried out using the Sparse Grid adaptive method in an integrated framework. The MOGA method was used for the optimization analysis in this paper. The final optimized model parameters were obtained, with 0.89% increase in efficiency and a 10.78 KPa increase in pressure increment compared to the original model.

The internal flow characteristics of the original model and the optimized model were compared and analyzed. We obtained a slight increase in the blade surface load of the optimized model and a slight increase in the static pressure at the pressure surface of the blade compared to the original model. In particular, the pressure increase near the impeller shroud is more obvious. The flow velocity in the impeller is reduced compared to the original model, and the flow velocity in the guide vane is slightly increased, which leads to an increase in the vortex in the exit area of the guide vane. The vortex within the impeller occurs mainly at the inlet, outlet, and rotating walls of the impeller. The vortex of the optimized model is slightly improved at the outlet. The turbulent energy dissipation in the optimized model is smaller compared to the original model, so the optimized model has higher efficiency.

We finally carried out an experimental study of the optimized model and obtained that the numerical simulation parameters of the optimized model matched the experimental parameters. Therefore, we conclude that the integrated design–meshing–numerical simulation proposed in this paper is effective.

Author Contributions: Conceptualization, methodology, software, writing—original draft, writing—review and editing, investigation, and software, C.P; Funding acquisition, X.Z. and Y.G., Methodology, C.P., X.Z., Y.C. and Y.G.; Visualization, Y.C., C.P., H.L. and S.H.; All authors have read and agreed to the published version of the manuscript.

Conflicts of Interest: The authors declare no conflict of interest.

Nomenclature

n_s	Specific speed	[rpm/min:m^3/s, m]
Q	Flow rate	[L/s]
H	Head	[m]
U_t	The circumferential velocity of the impeller shroud	[m/s]
V_m	Axial component of absolute velocity	[m/s]
n	Rotation speed of impeller	[rpm/min]
a_1	Shroud diameter of impeller	[m]
a_2	Hub inlet diameter of impeller	[m]
h_t	Inlet hub ratio of impeller	[-]
a_3	Hub outlet diameter of impeller	[m]
h_v	Shroud length diameter ratio of impeller	[-]
a_4	Hub length of impeller	[m]
a_5	Number of impellers	[-]
a_6	Inlet angle of impeller	[°]
V	Velocity at which the fluid enters the impeller	[m]
r	Radius of the impeller	[m]
a_7	Hub outlet flow angle of impeller	[°]
a_8	Wrap angle of impeller	[°]
a_9	Tip clearance of impeller	[mm]
σ_{max}	Maximum blade thickness	[mm]
X	The set of x-coordinates of all points	[-]
Y	The set of y-coordinates of all points	[-]
N	The total number of points	[-]
W_l	The layered incremental space	[-]
V_l	The response function space for the full grid model	[-]
$V_{O,n}^S$	Response function space of the Sparse Grid model	[-]
$y+$	Dimensionless wall distance	[-]

Greek Letters

Ψ	Head coefficient	[-]
Φ	Inlet flow coefficient	[-]
γ	Hub half cone angle	[°]
σ	Pearson correlation coefficient	[-]

Abbreviations

GVF	Gas volume fraction	[%]
SRMP	Synchronal rotary multiphase pump	[-]
CFD	Computational fluid dynamics	[-]
MOGA	Multi-objective genetic algorithm	[-]
SST	Shear stress transport	[-]
CCD	Central composite design	[-]

References

1. Makogon, Y.F. Natural gas hydrates—A promising source of energy. *J. Nat. Gas Sci. Eng.* **2010**, *2*, 49–59. [CrossRef]
2. Yongchen, S.; Lei, Y.; Jiafei, Z.; Weiguo, L.; Mingjun, Y.; Yanghui, L.; Yu, L.; Qingping, L. The status of natural gas hydrate research in China: A review. *Renew. Sust Energ Rev.* **2014**, *31*, 778–791.
3. Shimizu, T.; Yamamoto, Y.; Tenma, N. Experimental Analysis of Two-Phase Flows and Turbine Pump Performance. *Int. J. Offshore Polar* **2016**, *26*, 371–377. [CrossRef]
4. Suh, J.; Kim, J.; Choi, Y.; Kim, J.; Joo, W.; Lee, K. Development of numerical Eulerian-Eulerian models for simulating multiphase pumps. *J. Pet. Sci. Eng.* **2018**, *162*, 588–601. [CrossRef]
5. Yu, Z.; Zhu, B.; Cao, S. Interphase force analysis for air-water bubbly flow in a multiphase rotodynamic pump. *Eng. Comput.* **2015**, *32*, 2166–2180. [CrossRef]
6. Yu, Z.; Zhu, B.; Cao, S.; Liu, Y. Effect of Virtual Mass Force on the Mixed Transport Process in a Multiphase Rotodynamic Pump. *Adv. Mech. Eng.* **2014**, *6*, 958352. [CrossRef]
7. Liu, M.; Cao, S.; Cao, S. Numerical analysis for interphase forces of gas-liquid flow in a multiphase pump. *Eng. Comput.* **2018**, *35*, 2386–2402. [CrossRef]
8. Zhang, W.; Yu, Z.; Zahid, M.; Li, Y. Study of the Gas Distribution in a Multiphase Rotodynamic Pump Based on Interphase Force Analysis. *Energies* **2018**, *11*, 1069. [CrossRef]
9. Zhang, W.; Yu, Z.; Li, Y. Application of a non-uniform bubble model in a multiphase rotodynamic pump. *J. Petrol. Sci. Eng.* **2019**, *173*, 1316–1322. [CrossRef]
10. Li, Y.; Yu, Z.; Zhang, W. Analysis of bubble distribution characteristics in a multiphase rotodynamic pump. *IOP Conf. Ser. Earth Environ. Sci.* **2019**, *240*, 62026. [CrossRef]
11. Zhang, J.Y.; Li, Y.J.; Cai, S.J.; Zhu, H.W.; Zhang, Y.X. Investigation on the gas pockets in a rotodynamic multiphase pump. *IOP Conf. Ser. Mater. Sci. Eng.* **2016**, *129*, 12007–12015. [CrossRef]
12. Wang, C.; Zhang, Y.; Zhang, J.; Zhu, J. Flow pattern recognition inside a rotodynamic multiphase pump via developed entropy production diagnostic model. *J. Pet. Sci. Eng.* **2020**, *194*, 107467. [CrossRef]
13. Huang, Z.; Shi, G.; Liu, X.; Wen, H. Effect of Flow Rate on Turbulence Dissipation Rate Distribution in a Multiphase Pump. *Processes* **2021**, *9*, 886. [CrossRef]
14. Jiang, Z.; Li, H.; Shi, G.; Liu, X. Flow Characteristics and Energy Loss within the Static Impeller of Multiphase Pump. *Processes* **2021**, *9*, 1025. [CrossRef]
15. Shi, G.; Liu, Z.; Xiao, Y.; Wang, Z.; Luo, Y.; Luo, K. Energy conversion characteristics of multiphase pump impeller analyzed based on blade load spectra. *Renew. Energy* **2020**, *157*, 9–23. [CrossRef]
16. Xu, Y.; Cao, S.L.; Reclari, M.; Wakai, T.; Sano, T. Multiphase performance and internal flow pattern of helico-axial pumps. *IOP Conf. Ser. Earth Environ. Sci.* **2019**, *240*, 32029. [CrossRef]
17. Yu, Z.Y.; Zhang, Q.Z.; Huang, R.; Cao, S.L. Numerical analysis of gas-liquid mixed transport process in a multiphase rotodynamic pump. *IOP Conf. Ser. Earth Environ. Sci.* **2012**, *15*, 32062. [CrossRef]
18. Xu, Y.; Cao, S.; Sano, T.; Wakai, T.; Reclari, M. Experimental Investigation on Transient Pressure Characteristics in a Helico-Axial Multiphase Pump. *Energies* **2019**, *12*, 461. [CrossRef]
19. Zhang, W.; Yu, Z.; Li, Y.; Yang, J.; Ye, Q. Numerical analysis of pressure fluctuation in a multiphase rotodynamic pump with air–water two-phase flow. *Oil Gas Sci. Technol.—Rev. Difp Energ. Nouv.* **2019**, *74*, 18. [CrossRef]
20. Zhang, J.; Fan, H.; Zhang, W.; Xie, Z. Energy performance and flow characteristics of a multiphase pump with different tip clearance sizes. *Adv. Mech. Eng.* **2019**, *11*, 2072051423. [CrossRef]
21. Shi, G.; Liu, Z.; Liu, X.; Xiao, Y.; Tang, X. Phase Distribution in the Tip Clearance of a Multiphase Pump at Multiple Operating Points and Its Effect on the Pressure Fluctuation Intensity. *Processes* **2021**, *9*, 556. [CrossRef]
22. Shi, G.; Yan, D.; Liu, X.; Xiao, Y.; Shu, Z. Effect of the Gas Volume Fraction on the Pressure Load of the Multiphase Pump Blade. *Processes* **2021**, *9*, 650. [CrossRef]

23.   Li, C.; Luo, X.; Feng, J.; Zhu, G.; Xue, Y. Effects of Gas-Volume Fractions on the External Characteristics and Pressure Fluctuation of a Multistage Mixed-Transport Pump. *Appl. Sci.* **2020**, *10*, 582. [CrossRef]

24.   Zhang, J.Y.; Zhu, H.W.; Ding, K.; Qiang, R. Study on measures to improve gas-liquid phase mixing in a multiphase pump impeller under high gas void fraction. *IOP Conf. Ser. Earth Environ. Sci.* **2012**, *15*, 62023. [CrossRef]

25.   Yang, X.; Hu, C.; Hu, Y.; Qu, Z. Theoretical and experimental study of a synchronal rotary multiphase pump at very high inlet gas volume fractions. *Appl. Eng.* **2017**, *110*, 710–719. [CrossRef]

26.   Shi, J.; Tao, S.; Shi, G.; Song, W. Effect of Gas Volume Fraction on the Energy Loss Characteristics of Multiphase Pumps at Each Cavitation Stage. *Water-Sui* **2021**, *13*, 2293. [CrossRef]

27.   Shi, G.; Wang, S.; Xiao, Y.; Liu, Z.; Li, H.; Liu, X. Effect of cavitation on energy conversion characteristics of a multiphase pump. *Renew. Energ.* **2021**, *177*, 1308–1320. [CrossRef]

28.   Liu, X.; Hu, Q.; Wang, H.; Jiang, Q.; Shi, G. Characteristics of unsteady excitation induced by cavitation in axial-flow oil–gas multiphase pumps. *Adv. Mech. Eng.* **2018**, *10*, 2072046214. [CrossRef]

29.   Zhang, Y.; Zhang, J.; Zhu, H.; Cai, S. 3D Blade Hydraulic Design Method of the Rotodynamic Multiphase Pump Impeller and Performance Research. *Adv. Mech. Eng.* **2014**, *6*, 803972. [CrossRef]

30.   Cao, S.; Peng, G.; Yu, Z. Hydrodynamic Design of Rotodynamic Pump Impeller for Multiphase Pumping by Combined Approach of Inverse Design and CFD Analysis. *J. Fluids Eng.* **2005**, *127*, 330–338. [CrossRef]

31.   Xiao, W.; Tan, L. Design method of controllable velocity moment and optimization of pressure fluctuation suppression for a multiphase pump. *Ocean Eng.* **2021**, *220*, 108402. [CrossRef]

32.   Liu, M.; Tan, L.; Cao, S. Design Method of Controllable Blade Angle and Orthogonal Optimization of Pressure Rise for a Multiphase Pump. *Energies* **2018**, *11*, 1048. [CrossRef]

33.   Shi, G.; Li, H.; Liu, X.; Liu, Z.; Wang, B. Transport Performance Improvement of a Multiphase Pump for Gas–Liquid Mixture Based on the Orthogonal Test Method. *Processes* **2021**, *9*, 1402. [CrossRef]

34.   Kim, J.; Lee, H.; Kim, J.; Choi, Y.; Yoon, J.; Yoo, I.; Choi, W. Improvement of Hydrodynamic Performance of a Multiphase Pump Using Design of Experiment Techniques. *J. Fluids Eng.* **2015**, *137*, 081301. [CrossRef]

35.   Suh, J.; Kim, J.; Choi, Y.; Joo, W.; Lee, K. A study on numerical optimization and performance verification of multiphase pump for offshore plant. *Proc. Inst. Mech. Eng. Part A J. Power Energy* **2017**, *231*, 382–397. [CrossRef]

36.   Zhang, J.; Zhu, H.; Yang, C.; Li, Y.; Wei, H. Multi-objective shape optimization of helico-axial multiphase pump impeller based on NSGA-II and ANN. *Energy Convers. Manag.* **2011**, *52*, 538–546. [CrossRef]

37.   Liu, M.; Tan, L.; Xu, Y.; Cao, S. Optimization design method of multi-stage multiphase pump based on Oseen vortex. *J Pet. Sci. Eng.* **2020**, *184*, 106532. [CrossRef]

38.   Mycek, P.S.S.; Gaurier, B.I.; Sup, T.S.; Germain, G.E.; Sup, G.S.; Pinon, G.E.; Sup, G.S.; Rivoalen, E.S.S. Experimental study of the turbulence intensity effects on marine current turbines behaviour. Part I: One single turbine. *Renew. Energy Int. J.* **2014**, *66*, 729–746. [CrossRef]

39.   Ma, D.; Duan, H.; Liu, W.; Ma, X.; Tao, M. Water–Sediment Two-Phase Flow Inrush Hazard in Rock Fractures of Overburden Strata During Coal Mining. *Mine Water Env.* **2020**, *39*, 308–319. [CrossRef]

40.   Ramezanizadeh, M.R.M.S.; Nazari, M.N.M.A.; Ahmadi, M.A.M.H.; Chau, K.C.K.S. Experimental and numerical analysis of a nanofluidic thermosyphon heat exchanger (Article). *Eng. Appl. Comp. Fluid Mech.* **2019**, *13*, 40–47.

41.   Wu, D.W.D.S.; Yuan, S.Y.S.S.; Ren, Y.R.Y.S.; Mu, J.M.J.S.; Yang, Y.Y.Y.S.; Liu, J.L.J.S. CFD investigation of the influence of volute geometrical variations on hydrodynamic characteristics of circulator pump. *Chin. J. Mech. Eng.* **2016**, *29*, 315–324. [CrossRef]

42.   Gravier, J.; Vignal, V.; Bissey-Breton, S.; Farre, J. The use of linear regression methods and Pearson's correlation matrix to identify mechanical–physical–chemical parameters controlling the micro-electrochemical behaviour of machined copper. *Corros. Sci.* **2008**, *50*, 2885–2894. [CrossRef]

43.   Sup, M.T.S.; Aemail, D.Z.S.S.; Sup, D.W.S.; Sup, J.D.S.; Sup, D.K.S.; Sup, H.Z.S. Performance prediction of 2D vertically stacked MoS_2-WS_2 heterostructures base on first-principles theory and Pearson correlation coefficient. *Appl. Surf. Sci.* **2022**, *596*, 153498.

44.   Butnaru, D.; Pflüger, D.; Bungartz, H. Towards High-Dimensional Computational Steering of Precomputed Simulation Data using Sparse Grids. *Procedia Comput. Sci.* **2011**, *4*, 56–65. [CrossRef]